Numerical study of the statistical properties of the lensing excursion angles

Takashi Hamana, Yannick Mellier

Mon. Not. R. Astron. Soc. **327,** 169–176 (2001)

Numerical study of the statistical properties of the lensing excursion angles

Takashi Hamana[1,2★†] and Yannick Mellier[1,3]

[1]*Institut d'Astrophysique de Paris, CNRS, 98bis Boulevard Arago, F75014 Paris, France*
[2]*Max-Planck-Institut für Astrophysik, PO Box 1317, D–85741 Garching, Germany*
[3]*Observatoire de Paris, DEMIRM, 61 avenue de l'Observatoire, 75014 Paris, France*

Accepted 2001 May 23. Received 2001 March 26; in original form 2001 January 24

ABSTRACT

We present ray tracing simulations combined with sets of large *N*-body simulations. Experiments were performed to explore, for the first time, the statistical properties of fluctuations in angular separation of nearby light-ray pairs (the so-called lensing excursion angle) induced by weak lensing by large-scale structures. We found that the probability distribution function (PDF) of the lensing excursion angles is not simply Gaussian, but has an exponential tail. It is found, however, that the tail, or more generally the non-Gaussian nature of the PDF has no significant impact on the weak lensing of the cosmic microwave background (CMB). Moreover, we found that the variance in the lensing excursion angles predicted by the power spectrum approach is in good agreement with our numerical results. These results demonstrate the validity of using the power spectrum approach to compute lensing effects on the CMB.

Key words: gravitational lensing – cosmology: theory – dark matter – large-scale structure of Universe.

1 INTRODUCTION

Weak lensing effects on the temperature anisotropy in the cosmic microwave background (CMB) have been recognized as a powerful probe of cosmology (see Mellier 1999; Bartelmann & Schneider 2001 for reviews). Dark-matter distribution along the line of sight between the last scattering surface (LSS) and us deflects the light-ray trajectories and induces distortions in the pattern of the CMB anisotropies. As the gravitational lensing is directly sensitive to the matter distribution up to the LSS, lensing signatures imprinted on the CMB may provide important information about the matter distribution on large scales and at high redshifts. From this point of view, various methods have been proposed (Seljak 1996; Bernardeau 1997, 1998; Metcalf & Silk 1997; Zaldarriaga & Seljak 1998, 1999; Suginohara, Suginohara & Spergel 1998; Van Waerbeke, Bernardeau & Benabed 2000; Takada, Komatsu & Futamase 2000; Zaldarriaga 2000; Takada & Futamase 2001). These lensing signatures are generally small, but are measurable with two planned satellite missions, *MAP*[1] and *Planck*,[2] and can help to break some of the parameter degeneracies in the CMB (Bernardeau 1997; Metcalf & Silk 1998; Takada & Futamase 2000). The change in a separation angle of two nearby light rays, caused by weak lensing (lensing excursion angle), plays a key role in studying weak lensing of the CMB, especially weak lensing effects on the two-point statistics of the CMB.

The analytical prediction of the weak lensing effect on the CMB power spectrum in modern cosmological models was first developed by Seljak (1994), based on linear perturbation theory (the so-called power spectrum approach). In his subsequent paper, Seljak (1996) examined the effects of the non-linearity in the density through analytic fitting formulae (Peacock & Dodds 1996), and pointed out that the non-linearity is very important on sub-degree scales. Furthermore, statistics of the lensing excursion angles caused by weak lensing are frequently assumed to be Gaussian without a rigorous basis (e.g. Seljak 1996). Therefore, numerical simulations are needed, therefore, for testing the validity and limitation of the semi-analytic approach.

The purpose of this paper is to examine the statistical properties of the lensing excursion angles using ray-tracing simulations combined with large *N*-body simulations for the first time. Because the simulations were originally constructed for the cosmic shear statistics (Van Waerbeke et al. 2001; Hamana et al. 2001b), the maximum redshift is taken as $z \sim 3$, which is about halfway to the LSS. This choice may not seem to be enough for studying the weak lensing effects on the CMB. However, most of the contributions to the CMB lensing come from structures at $z < 3$. To take an example shown by Suginohara et al. (1998), in standard cold dark matter (SCDM) model, normalized by the *Cosmic Background Explorer* (*COBE*) data, the structures within $z < 3$ contribute 85 per cent to the variance of the lensing angular excursion from the LSS (see fig. 1b of their paper). The remaining 15 per cent will not significantly alter the basic properties of weak lensing of the CMB,

★E-mail: hamana@yukawa.kyoto-u.ac.jp
†Present address: National Astronomical Observatory, Mitaka, Tokyo 181-8588, Japan.

[1] See the *MAP* homepage at http://map.gsfc.nasa.gov
[2] See the *Planck* homepage at http://astro.estec.esa.nl/*Planck*

and therefore we can, at least, study its essential features. It should be noticed, however, that this 15 per cent is surely the most interesting for probing the early stage of the large-scale structure formation with weak lensing of the CMB.

The outline of this paper is as follows. Our models and method of the ray-tracing simulation are described in Section 2. In Section 3, we show the numerical resolution of our simulation and discuss its limitation. Using the results of the ray-tracing simulations, we examine the statistical properties of the lensing excursion angles in Section 4. We conclude in Section 5.

Throughout this paper, we work in the comoving coordinates system. The cosmological parameters are denoted with usual notations; Hubble constant, $H_0 = 100\,h\,\mathrm{km\,s^{-1}\,Mpc^{-1}}$; the density parameter, Ω_m; the cosmological constant, Ω_Λ; the variance of the density fluctuation in a sphere of radius $8\,h^{-1}\,\mathrm{Mpc}$, σ_8^2.

2 NUMERICAL METHODS AND MODELS

In this section, we describe methods of the *N*-body simulation (Section 2.1) and the ray-tracing simulation (Section 2.2), and summarize our models.

2.1 *N*-body simulation and the tiling technique

The *N*-body simulation data set were generated with a particle mesh (PM) code (see Hamana et al. 2001b for a detailed description). Each *N*-body experiment involves $256^2 \times 512$ particles in a periodic rectangular box of size (L, L, $2L$). The mesh used to compute the forces was $256^2 \times 512$. The initial conditions are generated adopting the transfer function of Bond & Efstathiou (1984) with the shape parameter $\Gamma = \Omega_\mathrm{m} h$. We adopt three cosmological models; two flat models with and without the cosmological constant and one open model. The amplitude of the power spectrum is normalized by the cluster abundance (Eke, Cole & Frenk 1996; Kitayama & Suto 1997). In Table 1, cosmological parameters in each model are summarized.

A light cone of the particles was extracted from each simulation during the run as explained in Hamana, Colombi & Suto (2001a). Our aim was that the light cone covers a large redshift range, $0 \leq z \lesssim 3$, and a field of view of 5×5 square degrees with a wide angular dynamic range. To do that, we adopted the *tiling* technique first proposed by White & Hu (2000). We performed $N_\mathrm{box} = 11$, 12 and 13 independent simulations for SCDM, OCDM and ΛCDM, respectively, covering adjacent redshift intervals $[z_i^\mathrm{min}, z_i^\mathrm{max}]$, $i = 1, \ldots, N_\mathrm{box}$. The size of each simulation is chosen such that the portion of the light cone in $[z_i^\mathrm{min}, z_i^\mathrm{max}]$ (aligned with the third axis) fits the box size as shown in Fig. 1. This way, angular resolution is approximately conserved as a function of redshift, except close to the observer (this will be discussed in Section 3). Finally, in order to keep large-scale modes that may contribute to the weak lensing, we impose the supplementary constraint $L \geq 80\,h^{-1}\,\mathrm{Mpc}$. As a result, L follows the sequence with redshift as summarized in Table 2.

Table 1. Cosmological parameters.

Model	Ω_m	Ω_λ	h	σ_8
SCDM	1.0	0.0	0.5	0.6
OCDM	0.3	0.0	0.7	0.85
ΛCDM	0.3	0.7	0.7	0.9

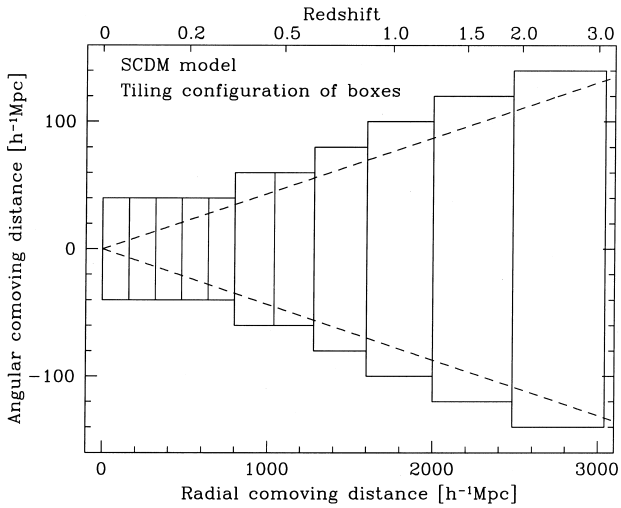

Figure 1. Tiling configuration of *N*-body simulation boxes for the SCDM model. Dashed lines (cone) show the comoving angular diameter distance of ±2.5 arcmin. Note that the scale of the vertical axis is exceedingly enlarged for clarity and the long side of the rectangular boxes is parallel to the horizontal axis.

Table 2. Characteristics of PM simulation boxes.

Model	L[a] $h^{-1}\,\mathrm{Mpc}$	m_part[b] $h^{-1}\,10^{10}\,\mathrm{M}_\odot$	Redshift range z_min	z_max
SCDM	80	0.85	0.0	0.055545
	80	0.85	0.055545	0.11585
	80	0.85	0.11585	0.18147
	80	0.85	0.18147	0.25306
	80	0.85	0.25306	0.33136
	120	2.9	0.33136	0.46332
	120	2.9	0.46332	0.61591
	160	6.8	0.61591	0.85950
	200	13	0.85950	1.2500
	240	23	1.2500	1.9054
	280	36	1.9054	3.1088
OCDM	80	0.25	0.0	0.055010
	80	0.25	0.055010	0.11355
	80	0.25	0.11355	0.17589
	80	0.25	0.17589	0.24235
	80	0.25	0.24235	0.31326
	120	0.86	0.31326	0.42880
	120	0.86	0.42880	0.55664
	160	2.0	0.55664	0.74917
	200	4.0	0.74917	1.0323
	240	6.9	1.0323	1.4508
	320	16	1.4508	2.1935
	440	42	2.1935	3.7702
ΛCDM	80	0.25	0.0	0.053997
	80	0.25	0.053997	0.10942
	80	0.25	0.10942	0.16641
	80	0.25	0.16641	0.22515
	80	0.25	0.22515	0.28581
	120	0.86	0.28581	0.38084
	120	0.86	0.38084	0.48137
	160	2.0	0.48137	0.62541
	200	4.0	0.62541	0.82485
	240	6.9	0.82485	1.1001
	280	11	1.1001	1.4870
	360	23	1.4870	2.1341
	440	42	2.1341	3.2942

[a]The short side length of boxes in comoving units, the long side length is $2L$ in all cases.
[b]Particle mass.

2.2 Ray-tracing simulation

Let us first summarize the basic equations of the multiple-lens plane algorithm which are directly relevant to this paper (see e.g. Schneider, Ehlers & Falco 1992 and Jain, Seljak & White 2000 for details). We shall denote the comoving Cartesian coordinate system as (x_1, x_2, y), with y being the third axis and the origin being at the observer point. Because the field of view we consider is small (5×5 square degrees), the radial comoving distance (we shall denote it by χ) can be approximated to y. In the standard multiple-lens plane algorithm, the distance between source and observer is divided into N intervals, separated by comoving distance Δy. The matter content in each interval is projected onto *lens planes* perpendicular to the y-axis. The projected density contrast of ith plane is defined by,

$$\delta_i^{\rm proj}(x_1, x_2) = \int_{y_{i-1}}^{y_i} {\rm d}y\, \delta(x_1, x_2, y), \tag{1}$$

where $\delta = \rho/\bar{\rho} - 1$ and y_i denotes the y-position of ith lens plane. The two-dimensional deflection potential of ith lens plane is related to the projected density contrast via the two-dimensional Poisson equation by

$$\nabla^2 \Psi^i(x_1, x_2) = \frac{8\pi G\bar{\rho}}{3c^2}\delta_i^{\rm proj}(x_1, x_2) = 3\Omega_{\rm m}\left(\frac{H_0}{c}\right)^2 \delta_i^{\rm proj}(x_1, x_2) \tag{2}$$

The light ray position on nth lens plane of a ray with image position $\boldsymbol{\theta}^1$ are computed using the multiple-lens plane equation,

$$\boldsymbol{\theta}^n = \boldsymbol{\theta}^1 - \sum_{i=1}^{n-1} \frac{f(\chi_n - \chi_i)}{a(\chi_i) f(\chi_n)} \nabla_\perp \Psi^i, \tag{3}$$

where $f(\chi)$ denotes the comoving angular diameter distance, defined as $f(\chi) = K^{-1/2}\sin K^{1/2}\chi$, χ and $(-K)^{-1/2}\sinh(-K)^{1/2}\chi$ for $K > 0$, $K = 0$ and $K < 0$, respectively, where K is the curvature, which can be expressed as $K = (H_0/c)^2(\Omega_{\rm m} + \Omega_\lambda - 1)$, and $\nabla_\perp$ denotes either $\partial/\partial x_1$ or $\partial/\partial x_2$. Note that the spatial position $\boldsymbol{x}^i$ on ith plane is related to the angular position by $\boldsymbol{x}^i = f(\chi_i)\boldsymbol{\theta}^i$. The evolution equation of the Jacobian matrix, which describes deformation of an infinitesimal light ray bundle, is written by

$$\mathsf{A}_n = \mathsf{I} - \sum_{i=1}^{n-1} \frac{f(\chi_i) f(\chi_n - \chi_i)}{a(\chi_i) f(\chi_n)} \mathsf{U}_i \mathsf{A}_i, \tag{4}$$

where I denotes the identity matrix, and U_i is the (so-called) optical tidal matrix, defined by

$$\mathsf{U}_i = \begin{pmatrix} \Psi^i_{,11} & \Psi^i_{,12} \\ \Psi^i_{,21} & \Psi^i_{,22} \end{pmatrix}, \tag{5}$$

with commas denoting the differentiation with respect to $\boldsymbol{x}$. It should be noticed that the first and second derivatives of Ψ in equations (3) and (4) must be evaluated at ray positions computed by the lens equation (3). The Jacobian matrix is usually decomposed into

$$\mathsf{A} = \begin{pmatrix} 1 - \kappa - \gamma_1 & -\gamma_2 - \omega \\ -\gamma_2 + \omega & 1 - \kappa + \gamma_1 \end{pmatrix}, \tag{6}$$

where κ represents convergence, $|\gamma| = (\gamma_1^2 + \gamma_2^2)^{1/2}$ is the amplitude of the shear of the light ray bundle, and ω is a net rotation of the beam.

We adopt a fixed interval between lens planes by $\Delta y = 80\,h^{-1}$ Mpc (for this choice, the long-side lengths of the simulation boxes are chosen so that they are multiples of $80\,h^{-1}$ Mpc). The procedure to trace light rays through N-body data with the multiple-lens plane algorithm can be described as follows: (i) computing the projected density contrast, $\delta_i^{\rm proj}$ from particle distribution in N-body data. (ii) computing the two-dimensional deflection potential, Ψ^i via Poisson equation (2) and evaluating the first and second derivatives of it. (iii) evaluating the distance combination for each lens plane and performing the summation in equations (3) and (4). In the rest of this section, we describe each step in some detail.

(i) A simulation particle located at a y-coordinate between y_{i-1} and y_i is projected onto the ith lens plane at y_i. This projection is performed in parallel to the third axis, and thus the (x_1, x_2) positions of the particle are not changed. Because the N-body data is periodic in $\boldsymbol{x}$ directions,[3] the projected particle distributions are also periodic. The projected density field is computed on a 512^2 square lattice from the projected particle distribution, using the triangular-shaped cloud (TSC) assignment scheme (Hockney & Eastwood 1988). In this step, the most important point is the choice of both the smoothing scheme and the grid size. Our main consideration when choosing them was to maintain the resolution provided by the N-body simulation and at the same time to remove shot noise caused by discreteness in N-body simulations by a relevant smoothing. We tested the smoothing scale by varying the size of grids: 256^2, 512^2 and 1024^2. In the case of the 1024^2 lattice, we found a white-noise contribution to the power spectrum of the lensing convergence at small scales, which is a typical signature of the discreteness effect (Jain et al. 2000). However, the discreteness effect was smoothed sufficiently well in both the 256^2 and the 512^2 lattice cases, so the white-noise contribution was not detected for those cases. On the other hand, we also found that the small-scale power was damped significantly for the 256^2 case, which indicates too much smoothing. We also tested another smoothing scheme, cloud-in-cell (Hockney & Eastwood 1988), with the same three grid sizes. In these cases, we found a non-negligible white-noise contribution. We therefore decided to adopt TSC with 512^2 lattice.

(ii) Poisson equation (2) is solved to compute Ψ^i using the fast Fourier transform method with the periodic boundary condition. The first and second derivatives of Ψ^i are evaluated on the lattice points using the usual finite difference method (see Appendix A of Premadi, Martel & Matzner 1998 for explicit expressions).

(iii) 512^2 rays are traced backward from the observer point. The initial ray directions are set on 512^2 grids, which correspond to pixels of angular size $5°/512 \sim 0.59$ arcmin. For each ray, we first computed ray positions on all the lens planes in an iterative manner, using the lens equation (3). The first and second derivatives of Ψ^i on a ray position are linearly interpolated from four nearest grids on which they were pre-computed (step ii). Finally, the summation in equation (4) is performed. The light-ray positions and four components of the Jacobian matrix on desired source planes are stored. Exact values of the source redshifts used in this paper are summarized in Table 3.

We performed 40 realizations of the underlying density field for each cosmological model by random shifts of the simulation boxes in the (x_1, x_2) directions using a periodic boundary condition. Note that the lens planes coming from the same box are shifted in the same way to maintain the clustering of matter in the box. It is important to note that the 40 realizations are not rigorously independent, because they come from the same set of simulation boxes. It is expected that the cosmic variance can not be correctly included because of this lack of independence, but this does not

[3] N-body simulation data is not periodic in the y-direction, because we used the light cone output.

Table 3. Exact values of the source redshifts. In the text, they are refereed to as $z_s = 1$, 2 and 3.

	SCDM	OCDM	ΛCDM
z_1	1.0025	1.0323	1.0034
z_2	2.0422	1.9836	1.9721
z_3	3.1088	2.9501	3.0419

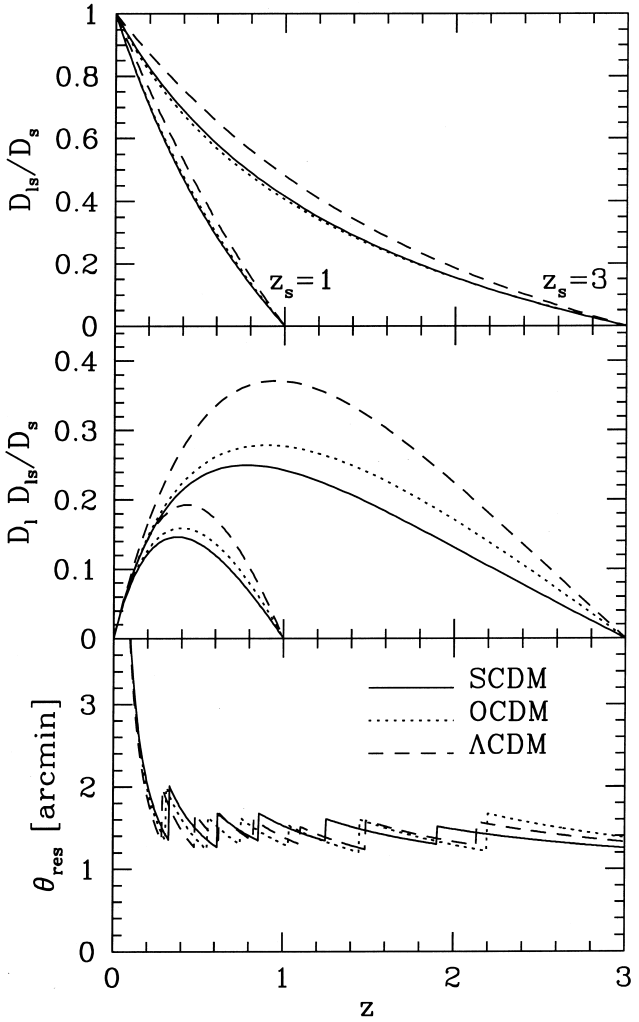

Figure 2. Top panel: Distance combination appearing in the equation (3) for $z_s = 1$ and 3 as a function of lens redshift. Middle panel: Distance combination appearing in the equation (4) (normalized by Hubble length, cH_0) for $z_s = 1$ and 3 as a function of lens redshift. Bottom panel: $\theta_{\rm res}$ as a function of redshift (see text).

change our results, because on angular scales of our interest (below 100 arcmin) it is very small.

3 NUMERICAL RESOLUTION

The angular resolution of the ray-tracing simulation is basically limited by the spatial resolution of the *N*-body simulations. As we used PM *N*-body code, the spatial resolution is simply $r_{\rm res} \simeq L/256$. This can be converted into the angular scale using the angular diameter distance relation, $r_{\rm res} = f(\chi)\theta_{\rm res}$. The bottom panel of Fig. 2 shows such angular scales computed for three cosmological models. Thanks to the tiling technique, $\theta_{\rm res}$ is almost constant ($\theta_{\rm res} \sim 1.5$ arcmin) at redshifts higher than 0.2. It increases as $\theta_{\rm res} \propto \chi^{-1}$ at $z \lesssim 0.2$, because of the constraint on the minimum box size. The impact of this worse resolution on a measurement depends on the quantity one wants to examine. Roughly speaking, quantities which come from solving the lens equation (3) are more influenced by the worse resolution than ones related to the Jacobian matrix obtained via equation (4).

The lensing excursion angle plays a crucial role in studies of the weak lensing effects on the CMB and it is defined by the difference in deflection angles between two nearby light rays. Each light-ray trajectory is computed by the lens equation. As the expression, equation (3), indicated, the distance combination $f(\chi_n - \chi_i)/f(\chi_n)$ acts as a weight function. The top panel of Fig. 2 shows this distance combination as a function of the lens redshift for two cases, $z_s = 1$ and 3, and clearly indicates that lensing deflections due to structures at low redshifts are more weighted than those by high redshift structures. It can therefore be expected that the poorer angular resolution at low redshifts has a significant impact on the effective accuracy of the light ray trajectory. In order to check it, we compute the variance in the lensing excursion angles of the two nearby light rays which would be observed with a separation θ if there was no lensing. The deflection angle of a light ray is simply the difference between its angular position in the first lens plane and that in the source plane, i.e., $\boldsymbol{\alpha} = \boldsymbol{\theta}^1 - \boldsymbol{\theta}^n$. The lensing excursion angle between nearby rays A and B is simply $\delta\boldsymbol{\alpha} = \boldsymbol{\alpha}^A - \boldsymbol{\alpha}^B$, and their intrinsic separation is $\theta = |\boldsymbol{\theta}^{n,A} - \boldsymbol{\theta}^{n,B}|$. In Fig. 3, the results are plotted together with the semi-analytic predictions by the power spectrum approach (Seljak 1994, 1996). The measurements agrees very well with the non-linear semi-analytic prediction at scales larger than 10 arcmin. Below that scale, the measurements are depressed, reflecting the effective resolution limit. We may conclude, therefore, that the angular range, where our analysis related to the lensing excursion angle is reliable, is between 10 arcmin and 2°.

Although we are not dealing with statistics of the lensing convergence in this paper, it is instructive to compare the effective resolution of the lensing convergence with that of the lensing excursion angle. The lensing convergence is computed by solving the evolution equation of the Jacobian matrix, equation (4). The distance combination appearing in this equation is $f(\chi_i)f(\chi_n - \chi_i)/f(\chi_n)$, and is shown in the middle panel in Fig. 2. This distance combination has a peak at intermediate redshift depending on the source redshift. Therefore, the poorer resolution at low-redshift lens planes has only small impact on the effective resolution of lensing signals, κ and γ, except for cases of very low source redshifts ($z_s \lesssim 0.5$). Fig. 4 shows that the two-point correlation function of the lensing convergence, defined by $C_\kappa(\theta) = \langle\kappa(\phi)\kappa(\phi + \theta)\rangle$, compared with the semi-analytic prediction (Bartelmann & Schneider 2001). The measurements agree well with the predictions, down to about 2 arcmin. Therefore, the effective resolution of the lensing convergence is found to be much better than that of the lensing excursion angle.

4 STATISTICAL PROPERTIES OF LENSING EXCURSION ANGLES

Fig. 5 shows the probability distribution function (PDF) of the lensing excursion angles normalized by its intrinsic separation. As the vector field $\boldsymbol{\delta\alpha}(\boldsymbol{\phi})$ has no special direction, we use both components, $\delta\alpha_1$ and $\delta\alpha_2$, to compute the PDFs. It is clearly shown in Fig. 5 that the PDFs consist of two contributions: a Gaussian

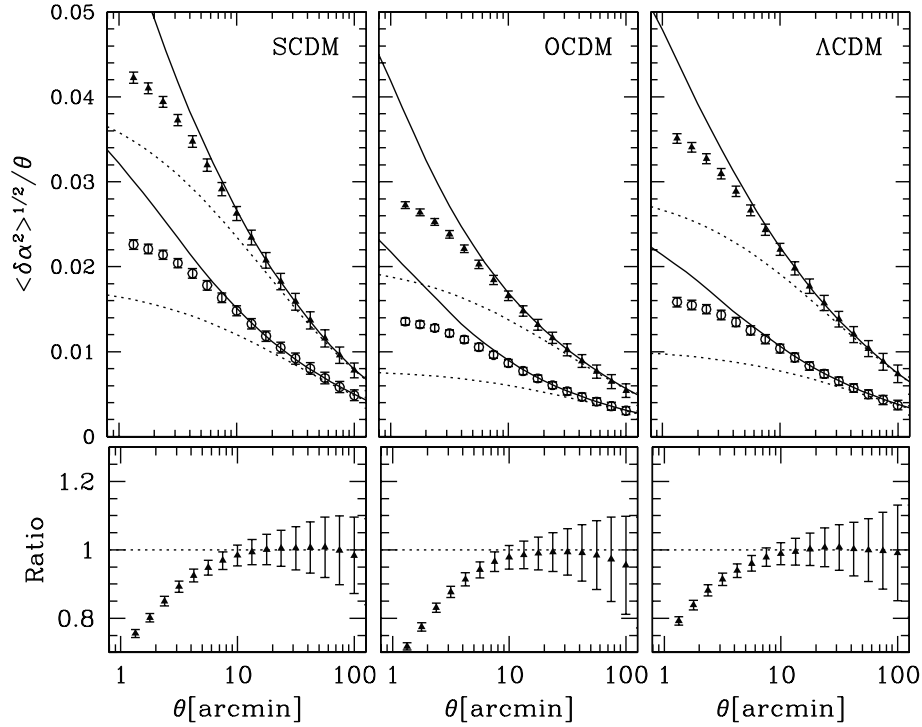

Figure 3. Top: The root mean square of lensing excursion angles between nearby light-ray pairs divided by their intrinsic separation θ. $\delta\alpha$ is either $\delta\alpha_1$ or $\delta\alpha_2$, and the average value is plotted. The open circles are for measurements of $z_s = 1$, while the filled triangles are for $z_s = 3$. The error bars denote the standard deviation computed among 40 realization. The solid and dotted lines represent the non-linear and linear prediction, respectively. Bottom: Ratio of the measurements to the non-linear prediction for $z_s = 3$.

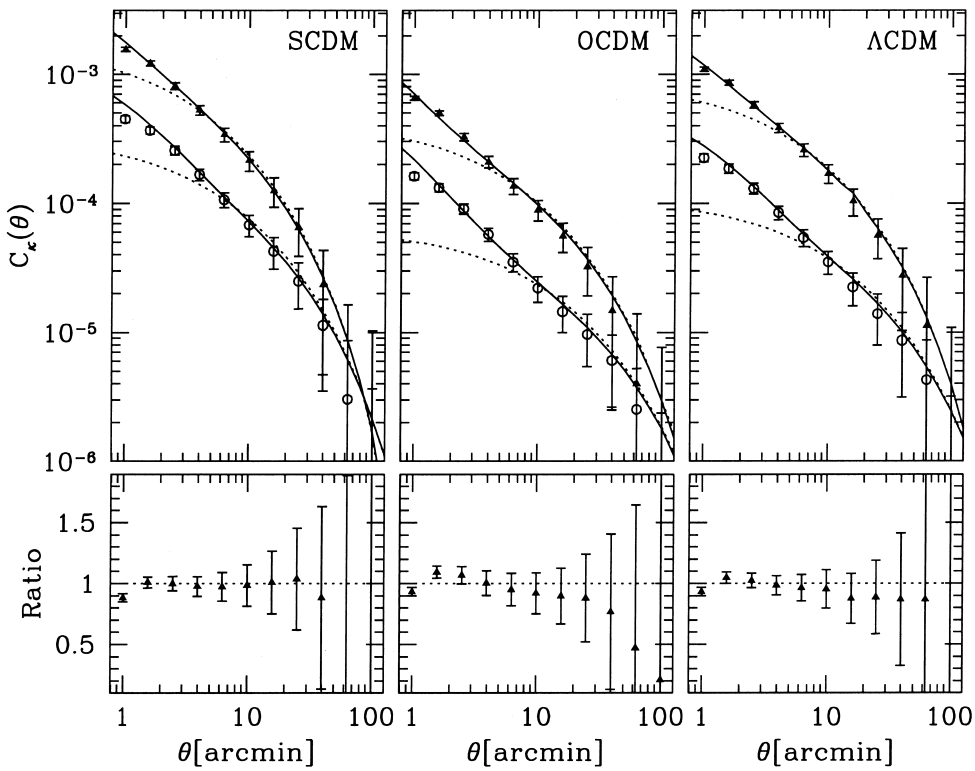

Figure 4. Same as Fig. 3, but for two-point correlation function of the lensing convergence.

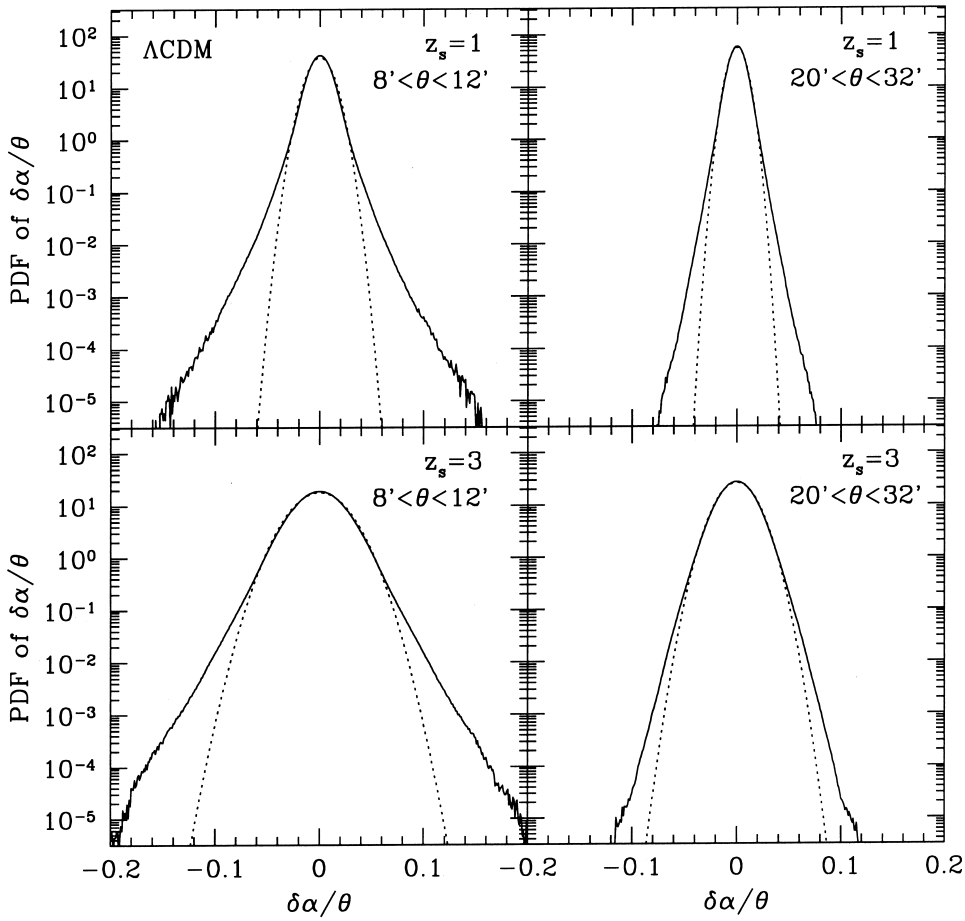

Figure 5. The probability distribution function of the lensing excursion angle normalized by its intrinsic separation (the solid curves). Top panels are for $z_s = 1$ and bottom panels for $z_s = 3$. Left and right panels are for light-ray pairs with intrinsic separation $8 < \theta < 12$ arcmin and $20 < \theta < 32$ arcmin, respectively. The dotted curves show Gaussian distribution with the σ computed the measured PDFs.

distribution at the inner part, and the exponential tail at the outer part. The inner part of the PDFs are fitted reasonably well by a Gaussian distribution with the σ computed from the PDFs (root-mean-square computed from the PDFs was used for σ). We should notice here that the measured standard deviation agrees very well with the semi-analytical prediction as shown in Fig. 3.

The fact that the PDFs consist of two contributions suggests that there are two different processes that make the lensing excursion angle. One, which makes Gaussian distribution, might be secular, small (random) deflections caused by linear density fluctuations along each light-ray path. This is explained by the fact that the lensing deflection angles, which are caused by Gaussian random fluctuations (such as the linearly evolved density fluctuation field), are Gaussian random field. As the light ray travels longer distances, the ray can undergo more fluctuations. Therefore the width of Gaussian distribution increases as the source redshift becomes higher. The other, which makes the exponential tail, might be a single (or possibly multiple) coherent scatter by a non-linear structure such as a galaxy or a cluster of galaxies.[4] As the separation of a light ray pair decreases, smaller scale, strongly non-linear structures can contribute to a coherent scatter. Therefore the exponential tail becomes more prominent for a small separation case than a larger one as shown in Fig. 5.

Does the exponential tail make a significant influence on studies of weak lensing effects on the CMB ? As far as the weak lensing effects on the CMB power spectrum concerned, it has no effect, because the crucial assumption that the lensing excursion angle is (in a statistical sense) much smaller than the intrinsic separation is true even in the presence of the exponential tail. This can not be directly demonstrated by our simulations as the light rays are not followed up to LSS, but can be proved by the semi-analytic prediction which tells that the root-mean-square of the lensing excursion angle is much smaller than the intrinsic separation angle. The validity of the semi-analytic prediction was supported by our numerical simulation (Fig. 3).

Fig. 6 shows the Kurtosis of the PDF of $\delta\alpha$ defined by $\langle\delta\alpha^4\rangle/\langle\delta\alpha^2\rangle^2 - 3$. The Kurtosis decreases as the source redshift becomes higher. On scales larger than 10 arcmin (below that, the lensing effects on the CMB will be hardly detected) the Kurtosis less than unity at $z_s = 3$, and thus, at the LSS, it must be smaller than that. It can be, therefore, said that the exponential tail or, more generally, the non-Gaussian nature in the PDF is very unlikely to have a significant effect on the weak lensing of the CMB.

[4] Computations of a lensing optical depth of strong lensing events by a galaxy or a clusters of galaxies as well as a small probability of finding multiple imaged quasi-stellar objects (QSOs) in a QSO catalogue tell us that light rays which undergo strong lensing more than two times are very rare (e.g. Chiba & Futamase 1999; Hattori, Kneib & Makino 1999, Hamana, Martel & Futamase 2000).

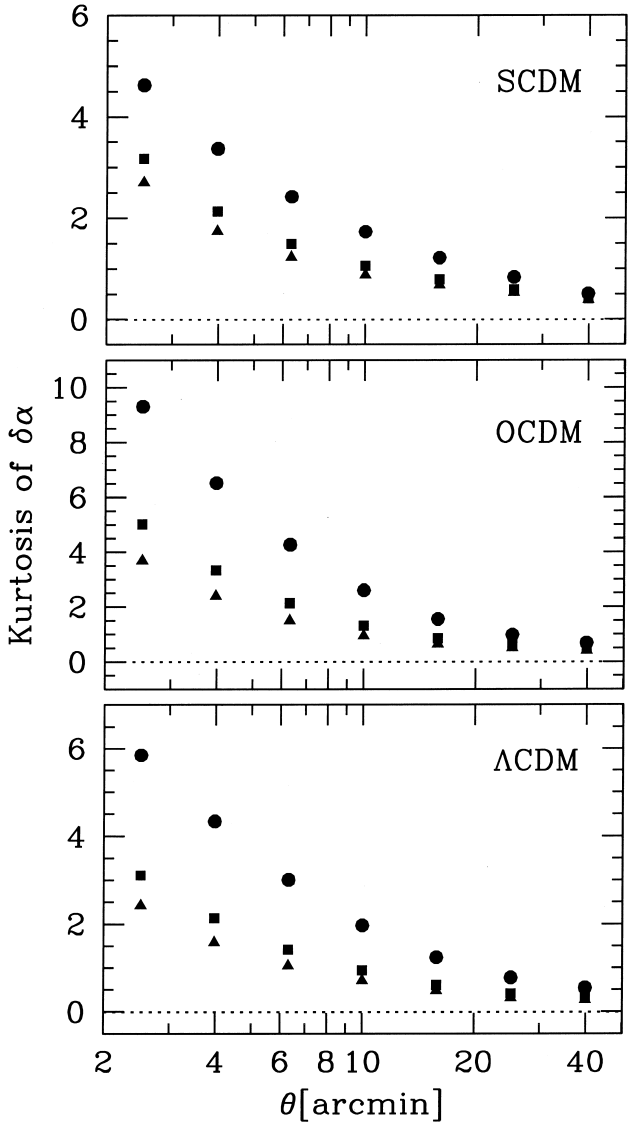

Figure 6. Kurtosis of lensing excursion angle $\delta\alpha$, that is, $\langle\delta\alpha^4\rangle/\langle\delta\alpha^2\rangle^2 - 3$, as a function of the intrinsic separation of light-ray pairs. Filled circles, filled squares and filled triangles are for measurements of $z_s = 1$, $z_s = 2$ and $z_s = 3$, respectively.

5 SUMMARY

We performed ray-tracing simulation combined with sets of large *N*-body simulations. The use of the tiling technique enable us to explore a wide angular dynamic range with the efficient PM *N*-body code. The angular resolution is limited by the spatial resolution that *N*-body simulations have. As the minimum box size is constrained to keep large-scale modes that may contribute to the weak lensing, the angular resolution of the low-redshift boxes becomes worse. We found that the tiling technique is particularly suitable for studying the cosmic shear statistics, because the poorer angular resolution does not make a serious impact on an effective angular resolution of the lensing convergence and shear. On the other hand, this worse resolution make a stronger effect on the effective resolution of the lensing excursion angles. One possible solution to improve the resolution is to use a higher resolution simulation such like P^3M code for a few lowest redshift boxes.

We have numerically examined the statistical properties of the lensing excursion angles. We found that the variance in the lensing excursion angles predicted by the power spectrum approach is in good agreement with our numerical results. We found that the PDF of the lensing excursion angles is not simply Gaussian but has an exponential tail. However, it can be safely concluded that the exponential tail, or more generally non-Gaussian nature in the PDF has no significant effects on the weak lensing of the CMB. These results demonstrate the validity of using the power spectrum approach to compute lensing effects on the CMB. Furthermore, our results support the validity of a simple numerical simulation method to obtain a lensed CMB map in which both the lensing displace filed and the CMB temperature map are generated assuming the Gaussian statistics and the lensed CMB map is obtained by a mapping (e.g. Takada & Futamase 2001).

ACKNOWLEDGMENTS

We acknowledge that the *N*-body simulations in this work were performed by S. Colombi, we thank him for his collaboration and for useful comments. We would like to thank M. Takada for fruitful discussions and an anonymous referee for a detailed report that have contributed to improvement of the manuscript. This research was supported in part by the Direction de la Recherche du Ministère Français de la Recherche. The computational means (CRAY-98) to do the *N*-body simulations were made available to us thanks to the scientific council of the Institut du Développement et des Ressources en Informatique Scientifique (IDRIS). Numerical computation in this work was partly carried out at IAP at the TERAPIX data centre and on MAGIQUE (SGI-02K).

REFERENCES

Bartelmann M., Schneider P., 2001, Physics Rep., 340, 291
Bernardeau F., 1997, A&A, 324, 15
Bernardeau F., 1998, A&A, 338, 767
Bond J. R., Efstathiou G., 1984, ApJ, 285, L45
Chiba M., Futamase T., 1999, Prog. Theor. Phys. S., 133, 115
Eke V. R., Cole S., Frenk C. S., 1996, MNRAS, 282, 263
Hamana T., Martel H., Futamase T., 2000, ApJ, 529, 56
Hamana T., Colombi S., Suto Y., 2001a, A&A, 367, 18
Hamana T., Colombi S., Thion A., Devriendt J., Mellier Y., Bernardeau F., 2001b, MNRAS, submitted (astro-ph/0012200)
Hattori M., Kneib J-P., Makino N., 1999, Prog. Theor. Phys. Supp., 133, 1
Hockney R. W., Eastwood J. W., 1988, Computer Simulation Using Particles. Adam Hilger, Bristol
Jain B., Seljak U., White S. D. M., 2000, ApJ, 530, 547
Kitayama T., Suto Y., 1997, ApJ, 490, 557
Mellier Y., 1999, ARA&A, 37, 127
Metcalf R. B., Silk J., 1997, ApJ, 489, 1
Peacock J. A., Dodds S. J., 1996, MNRAS, 280, L19
Premadi P., Martel H., Matzner R., 1998, ApJ, 493, 10
Seljak U., 1994, ApJ, 436, 509
Seljak U., 1996, ApJ, 463, 1
Schneider P., Ehlers J., Falco C. C., 1992, Gravitational Lenses. Springer-Verlag, New York
Suginohara M., Suginohara T., Spergel D. N., 1998, ApJ, 469, 437
Takada M., Komatsu E., Futamase T., 2000, ApJ, 533, L83
Takada M., Futamase T., 2001, ApJ, 546, 620

Van Waerbeke L., Bernardeau F., Benabed Y., 2000, ApJ, 540, 14
Van Waerbeke L., Hamana T., Scoccimarro R., Colombi S., Bernardeau F., 2001, MNRAS, 322, 918
White M., Hu W., 2000, ApJ, 537, 1
Zaldarriaga M., 2000, Phys. Rev. D, 62, 063510
Zaldarriaga M., Seljak U., 1998, Phys. Rev. D, 58, 023003
Zaldarriaga M., Seljak U., 1999, Phys. Rev. D, 59, 123507

This paper has been typeset from a TEX/LATEX file prepared by the author.